

ADVANCED MATERIALS

Supporting Information

for *Adv. Mater.*, DOI: 10.1002/adma.202003479

Discovery of Real-Space Topological Ferroelectricity in
Metallic Transition Metal Phosphides

Xian-Kui Wei, Gustav Bihlmayer, Xiaodong Zhou, Wanxiang
Feng, Yury V. Kolen'ko, Dehua Xiong, Lifeng Liu, Stefan
Blügel, and Rafal E. Dunin-Borkowski*

Supporting Information

Discovery of Real-Space Topological Ferroelectricity in Metallic Transition Metal Phosphides

*Xian-Kui Wei**, *Gustav Bihlmayer*, *Xiaodong Zhou*, *Wanxiang Feng*, *Yury V. Kolen'ko*,
Dehua Xiong, *Lifeng Liu*, *Stefan Blügel*, *Rafal E. Dunin-Borkowski*

*Corresponding author E-mail: x.wei@fz-juelich.de (X.-K.W.)

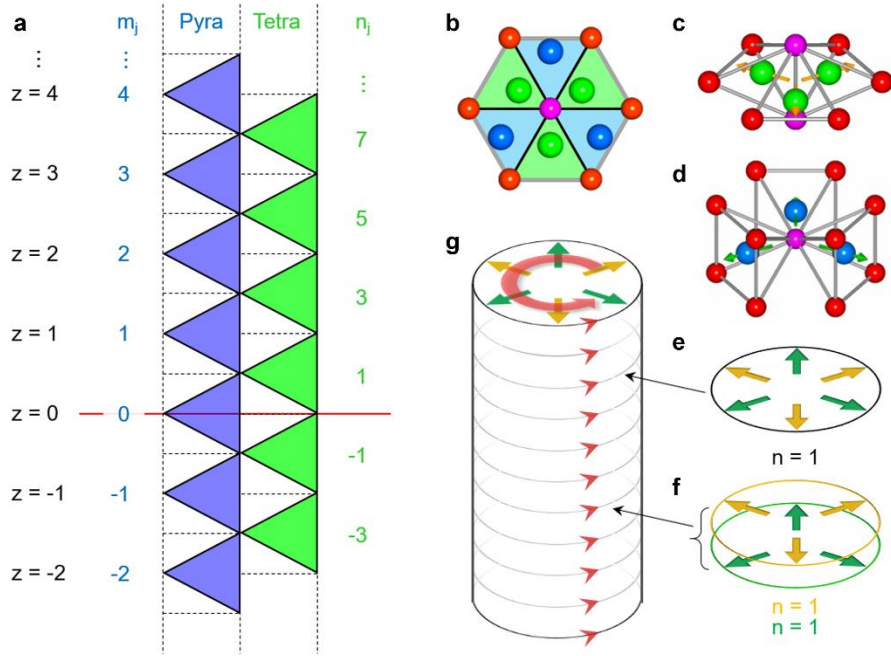


Figure S1. a) Relationship between out-of-plane (OP) polyhedral polarity associated with the values of m_j and n_j . b) Equal division of the equivalently-transformed unit cell (ETUC) by polyhedra-occupying triangular prisms (dashed rectangles in (a)) viewed along the [001] direction. The volume of the triangular prism with $V = V_0/6 = V_{Py} + V_{Te}$ (where $V_{Py} = 2V_{Te}$ and $V_0 \approx 0.10054 \text{ nm}^3$ is the volume of Ni₂P) is used to convert the Debye dipole moment into the volume polarization. c,d) Dipole geometry in the tetrahedra and pyramids, respectively. e,f) Polyhedral dipole configuration comprised of (e) combined and (f) separated tetrahedral and pyramidal units per unit cell, respectively. g) The counter map of polyhedral dipoles in the order-parameter space for Ni₂P with a $1 \times 1 \times z$ dimension. The homotopic mappings of closed contours along z axis give rise to an overall winding number of $n = 1$.

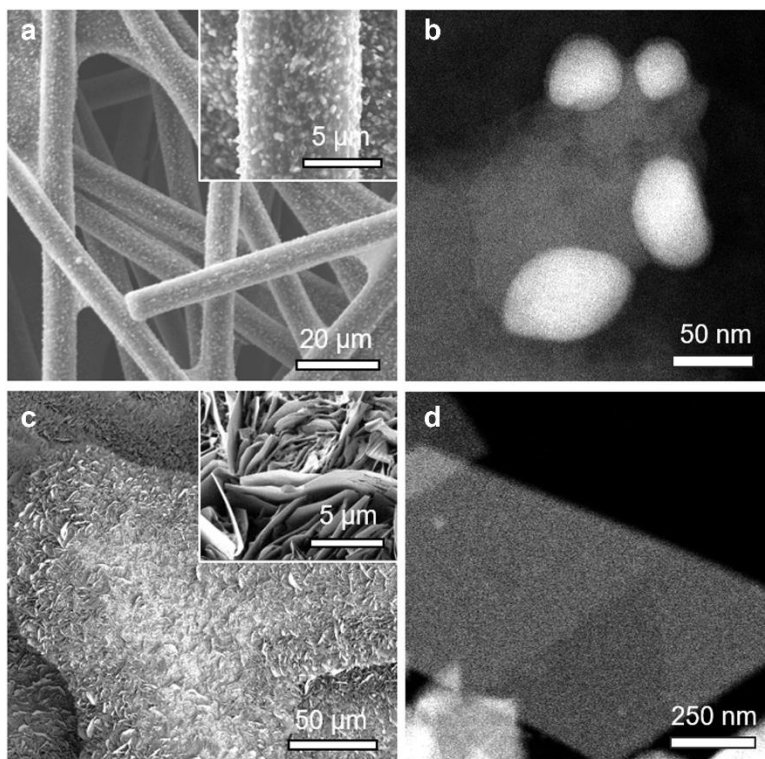


Figure S2. a,c) Scanning electron microscopy images and magnified views (insets) of (a) Ni₂P nanoparticles and (c) nanosheets comprised of mixed Ni₂P and Ni₅P₄ phases. b,d) Low magnification high-angle annular-dark-field scanning transmission electron microscopy images of (c) Ni₂P nanoparticles and (d) nanosheets. The nanoparticles in (c) are anchored to a (Mg,Ni)P_xO_y support that exhibits darker contrast.

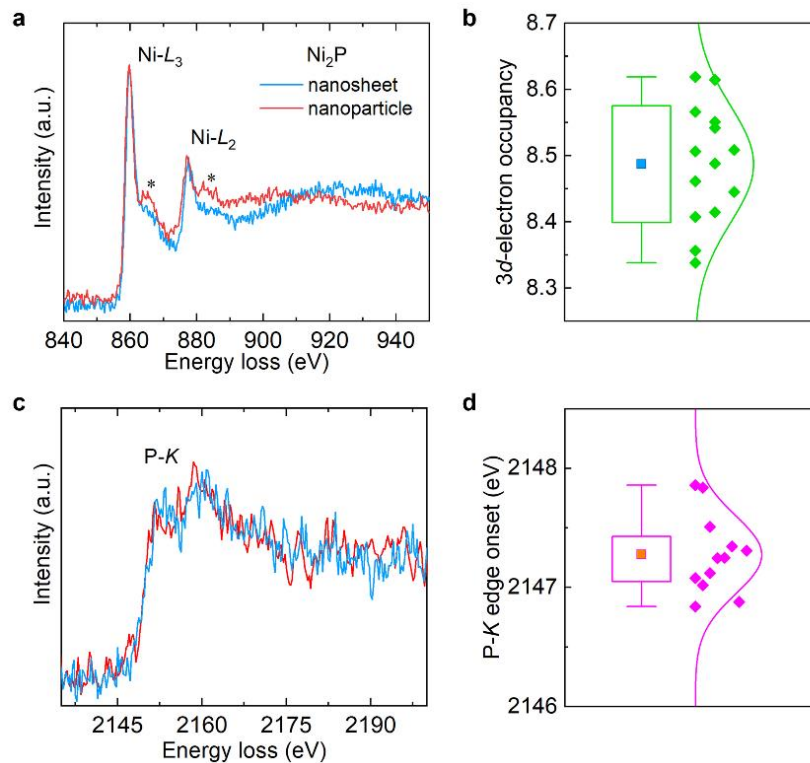


Figure S3. a,c) Representative (a) Ni $L_{2,3}$ and (c) P K edges in background-subtracted electron energy-loss spectra recorded from Ni₂P nanoparticle and nanosheet. The asterisks (*) in (a) mark shoulders arising from oxidized surfaces. It is seen that the Ni and P individually adopt the same electronic edge features despite the different sample morphologies. b,d) Statistical analysis of (b) 3d electron occupancy for Ni and (d) K edge onset energy for P in Ni₂P.

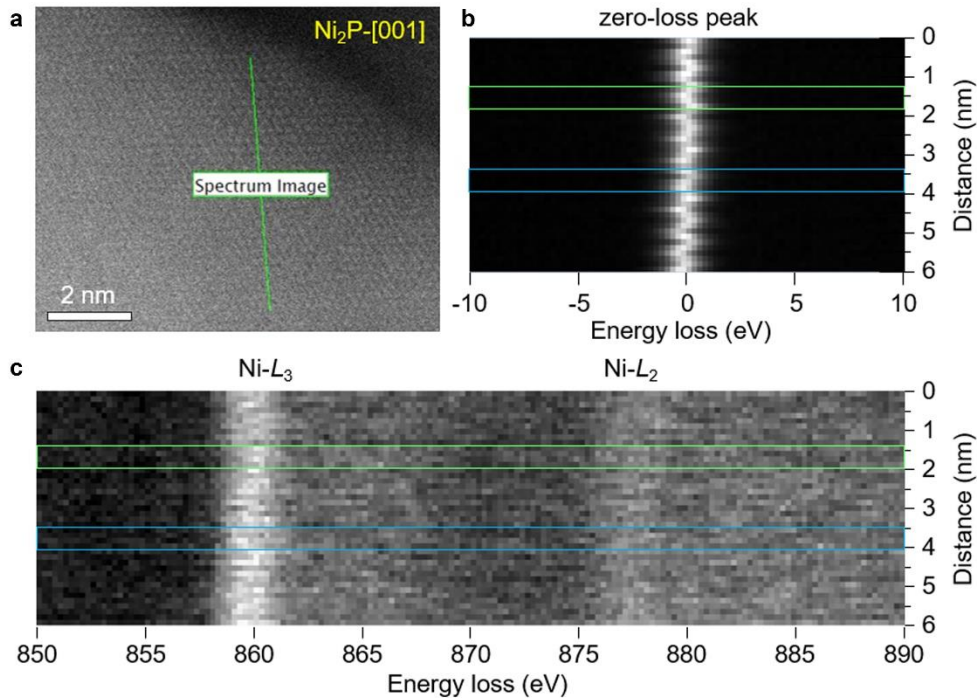


Figure S4. a) Atomic-scale high-angle annular-dark-field scanning transmission electron microscopy image of a Ni₂P particle along the [001] direction. b,c) Zero loss peak and Ni L_{2,3} core-loss edges recorded along the marked line in (a). The step size is 0.14 nm and the energy dispersion is 0.25 eV/pixel. In order to reduce signal noise, a binning of 4 was used for analysis of the data. The zero loss peak is essentially located at 0.00 ± 0.07 eV, which is much smaller than the peak gap of 0.75 eV. Changes in the positions of the Ni L₃ peaks along the energy-loss axis arise from changes in Ni valence in the scanning direction. The results shown in Figure 2b were extracted from the green and blue rectangles marked in (c).

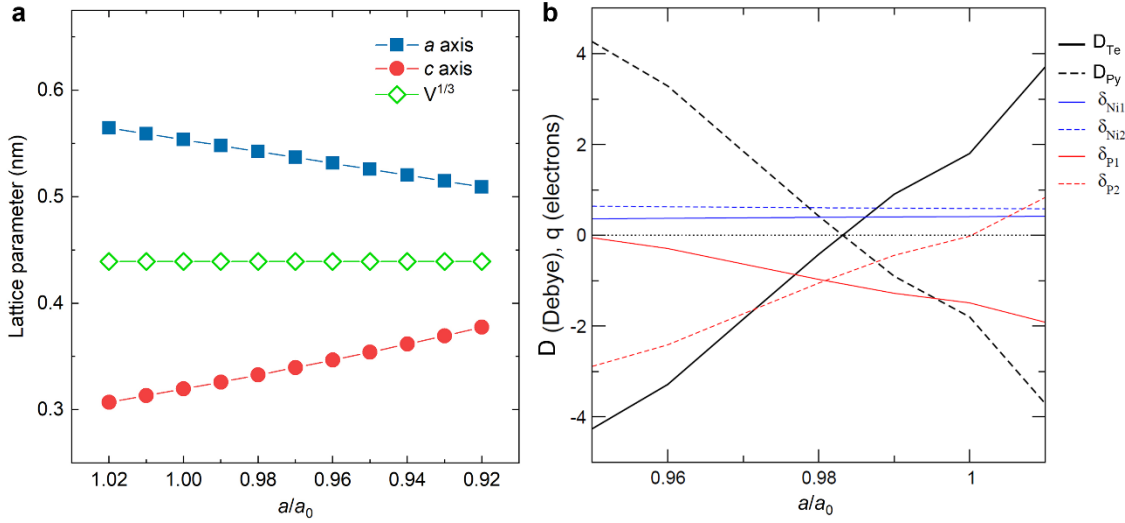


Figure S5. a) Change in lattice parameter and volume as a function of in-plane biaxial compressive strain. b) Change in tetrahedral and pyramidal dipole moment (D_{Te} , D_{Py}) and Ni, P valence as a function of in-plane compressive strain. A 1.7% reduction in the in-plane lattice parameter is sufficient to reverse the polyhedral polarity. Although the change in (x_{Ni1}, x_{Ni2}) is on the order of 1%, the effect on the nominal valence, in particular that of the P atoms, is sufficient to cause polarity reversal. It should be noted that the actual change in the P atomic sphere is much smaller than the variation in valence indicated here, since the spheres cover only a small fraction of the unit cell volume. The obtained polarization values this way are overestimated owing to assumption of point-localized charges. In addition, there remains a certain ambiguity in the definition of the valences δ , since their average values for the Ni atoms was fixed (see Experimental Section).

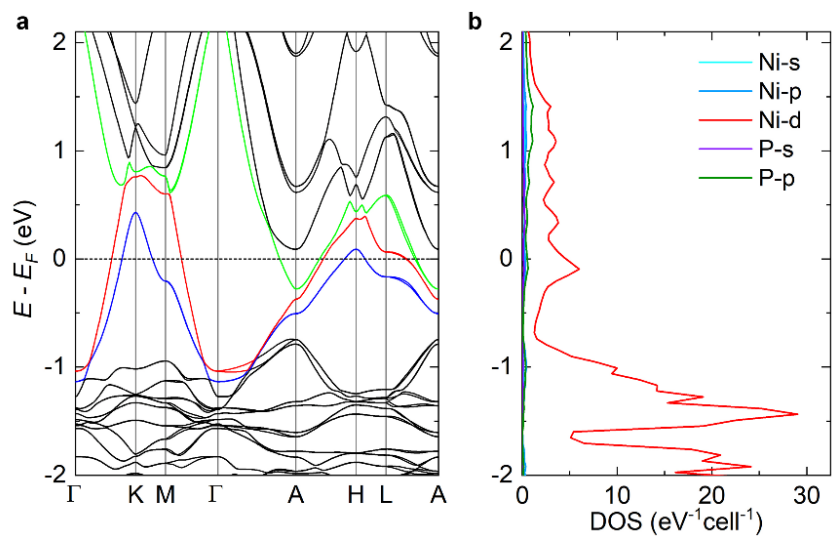


Figure S6. First-principles-calculated (a) band structure and (b) density of states (DOS) for Ni_2P at the $a = a_0$ condition. The energy dispersion curves crossing the Fermi level are highlighted by different colors. The DOS data provide evidence for the dominant influence of Ni-Ni bonding on Ni_2P metallicity.

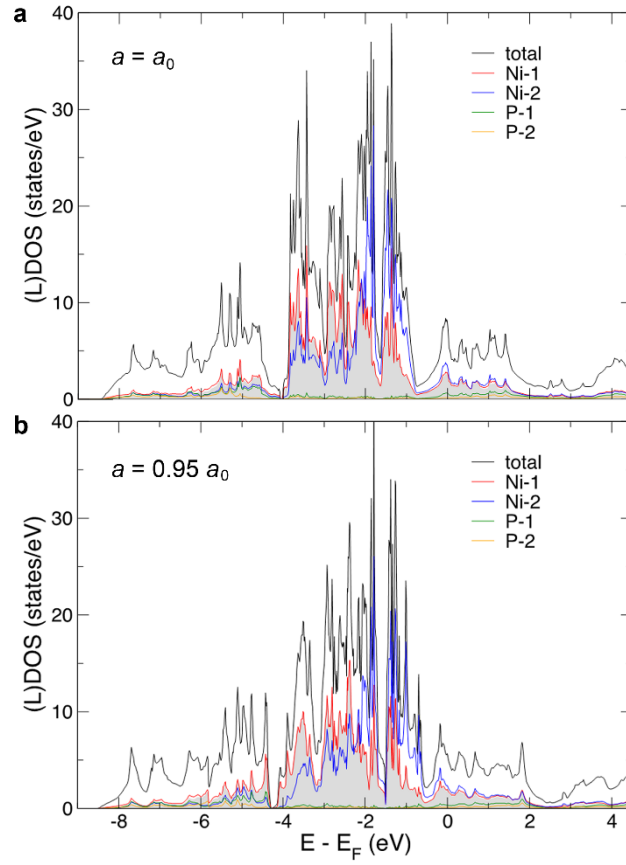


Figure S7. a,b) Total and local density of states (DOS) of Ni_2P for equilibrium ($a = a_0$) and reduced ($a = 0.95 a_0$) lattice constants, respectively. In both cases, the DOS at the Fermi level (E_F) is dominated by the Ni-1 and Ni-2 states, which are almost exclusively of d -character, as indicated by the grey shaded area (partial Ni-1- d DOS).

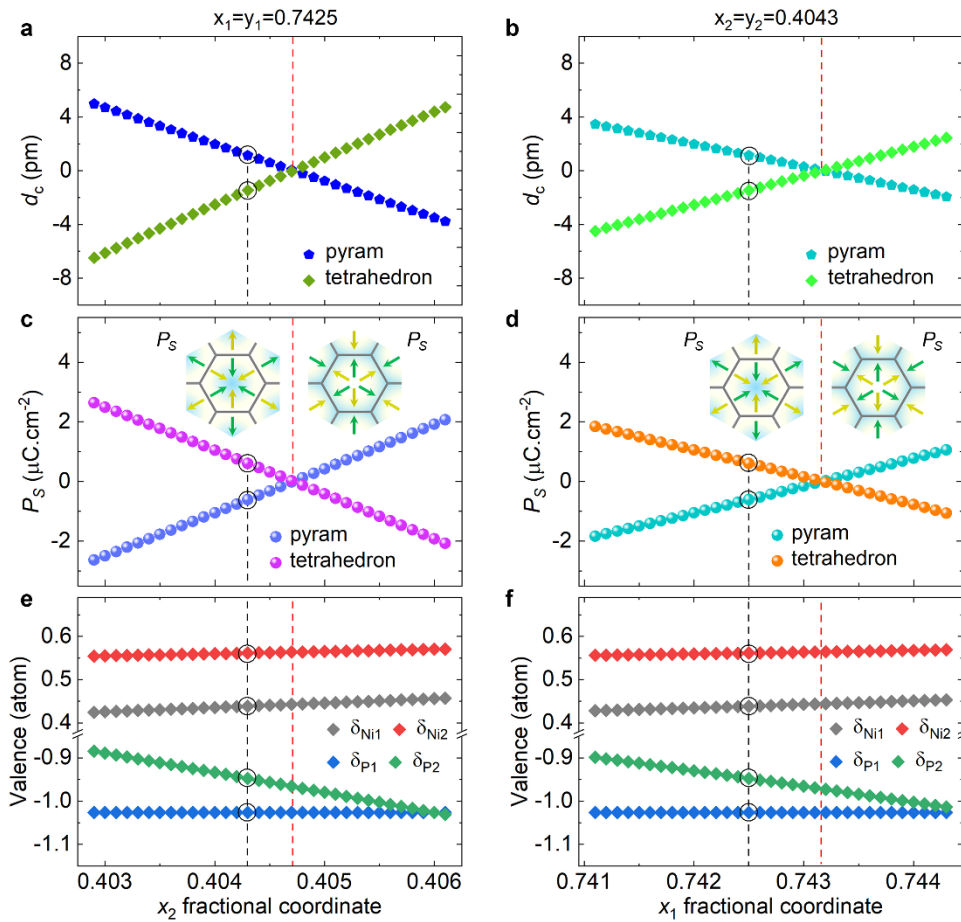


Figure S8. a,c,e) Changes of $d_{c\text{-Te/Py}}$ and polarization for the polyhedra and valence state as a function of varying $x_2 = y_2$ with fixed $x_1 = y_1 = 0.7425$. b,d,f) Change of $d_{c\text{-Te/Py}}$ and polarization for the polyhedra and valence state as a function of varying $x_1 = y_1$ with fixed $x_2 = x_2 = 0.4043$. The illustrated valence states are derived from a fixed P1 valence with $\delta_{P1} = -1.03$. The black dashed lines mark the atomic positions of Ni1 and Ni2 from DataSet-1, corresponding to the tetrahedral and pyramidal units highlighted in the primitive UC shown in Figure 1b. The red dashed lines mark the critical points of Ni fractional coordinates for polarity reversal (see insets in (c) and (d)).

Table S1. Atomic fractional coordinates, bond lengths and bond angles for hexagonal Ni₂P (Space group $P\bar{6}2m$) with $a = 0.5859$ nm and $c = 0.3382$ nm. The bond lengths are, by default, measured within the polyhedra and the ETUC, beyond which the information is indicated “B”. The polyhedral polarity is manifested by clear deviation of the bond angles, e.g., $\angle P-Ni1-P$ and $\angle P-P-P$, away from 109.47° and 60° .

Atomic coordinate	x	y	z	B factor/[\AA^2]
Ni1	x_1	y_1	0.5000	0.32
Ni2	x_2	y_2	0.5000	0.69
P1	1/3	2/3	0.5000	0.42
P2	0.0000	0.0000	0.5000	0.42

Bond length/nm		Bond length/nm		Tetrahedron/degree	
Ni1-P1	0.2209	Ni1-Ni2	0.2678	$\angle P1-Ni1-P1$	99.93
Ni1-P2	0.2266	Ni2-Ni2 ^B	0.3086	$\angle P2-Ni1-P2$	96.52
Ni2-P2	0.2369	P2-P2	0.3382	$\angle P1-Ni1-P2$	115.36
Ni2-P1	0.2457	P1-P1	0.3383	$\angle P1-P2-P1$	53.13
Ni1-Ni2 ^B	0.2605	Ni1-Ni1 ^B	0.3826	$\angle P2-P1-P2$	53.12
Ni1-Ni1	0.2613	Ni2-Ni2	0.4103	$\angle P1-P2-P2$	63.44

Note: The structural information is taken from DataSet-1, in which $x_1 = y_1 = 0.7425$ and $x_2 = y_2 = 0.4043$. Specifically, the selection of atoms and their positions depends on the polyhedra used for establishing the polarity symmetry equations. Along the $\langle 100 \rangle$ directions, the lattice symmetry gives rise to the same results.

Table S2. Summary of XPS-P $2p_{3/2}$ binding energy (E_B) for various ionic and covalent P-containing compounds with different valence states of P. A bowknot-shaped chart is concluded from the E_B -valence state relation summarized here.

P^{5+} species	E_B/eV	Ref.	P^{3+} species	E_B/eV	Ref.	$P^{\delta-}$ species	E_B/eV	Ref.
SbOPO ₄	137.8	[32]	PF ₃	135.0	[28]	BP ³⁻	129.9	[33]
NH ₄ PF ₆	137.65	[29]	H ₃ PO ₃	134.3	[34]	BNP ³⁻	129.3	[35]
P ₄ O ₁₀	135.6	[34]	PCl ₃	133.9	[36]	ScP ³⁻	127.7	[30,31]
BPO ₄	135.25	[29]	P ₂ O ₃	133.0	[37]	TiP ^{2.6-}	128.4	[30,31]
P ₂ O ₅	135.3	[34]	Na ₂ HPO ₃	132.9	[38]	VP ^{1.9-}	129.1	[30,31]
H ₃ PO ₄	135.2	[34]	P(CH ₃) ₃	131.3	[28]	CrP ^{1.4-}	129.1	[30]
FePO ₄	135.0	[39]	PH ₃	131.0	[28]	MnP ^{1.1-}	129.2	[30]
NaH ₂ PO ₄	134.3	[40]	P ⁰			MnP ^{1.1-}	129.4	[31]
SbPO ₄	133.9	[32]	P ⁰	130.45	[29]	FeP ¹⁻	129.3	[30]
Na ₂ HPO ₄	133.7	[40]	P ⁰	130.2	[34]	FeP ¹⁻	129.5	[31]
Ni ₃ (PO ₄) ₂	133.5	[29]	P ⁰	130.0	[38]	CoP ^{0.7-}	129.5	[30]
LiFePO ₄	133.46	[41]	P ⁰	129.9	[31]	Ni ₂ P ¹⁻	129.4	[26]
LiFeP ₄ O ₇	133.4	[42]	P ⁰	129.8	[37]	P ⁴⁺		
Na ₃ PO ₄	133.0	[40]	P ¹⁺			PO ₂	132.67	[43]
Na ₃ PO ₄	132.75	[29]	<i>p</i> -P ₄ O ₂	131.54	[43]	P(CH ₃ O) ₃	133.2	[44]